

1 **Automated Processing of Oceanic Bubble Images for measuring Bubble Size**
2 **Distributions underneath Breaking Waves**

3 Raied S. Al-Lashi^{*}, Steve R. Gunn^{**}, and Helen Czerski^{***}

4 ^{*} School of Food Science and Nutrition, Faculty of Mathematics and Physical Sciences,
5 University of Leeds, UK.

6 ^{**} Electronics and Computer Science (ECS), Faculty of Physical Sciences and Engineering,
7 University of Southampton, UK

8 ^{***} Department of Mechanical Engineering, University College London (UCL), UK.

9 **Correspondence Email: R.Al-lashi@leeds.ac.uk**

10

11 **ABSTRACT**

12 Accurate, in situ measurements of oceanic bubble size distributions beneath breaking waves
13 are needed for a better understanding of air-sea gas transfer and aerosol production processes.

14 To achieve this goal, a novel high-resolution optical instrument for imaging oceanic bubbles
15 was designed and built in 2013 for the HiWINGS campaign in the North Atlantic Ocean. The

16 instrument is able to operate autonomously and can continuously capture high resolution
17 images at 15 frames/sec over an 8 hour deployment. The large number of images means that it

18 is essential to use an automated processing algorithm to process these images. This paper
19 describes an automated algorithm for processing oceanic images based on a robust feature

20 extraction technique. The main advantages of this robust algorithm are it is significantly less
21 sensitive to the noise and insusceptible to the background changes in illumination, can extract

22 bubbles as small as 1 pixel (approximately 20 μm) in radius accurately, has low computing
23 time (approximately 5 seconds per image), and is simple to implement. The algorithm was

24 successfully used to analyse a large number of images (850000 images) from deployment in
25 the North Atlantic Ocean as part of the HiWINGS campaign in 2013.

26

27 **1. Introduction**

28 Bubble plumes entrained by breaking waves in the open ocean have a significant influence on
29 various oceanographic phenomena, including air sea gas transfer (Farmer et al., 1993,
30 Wanninkhof et al., 2009), marine aerosol production (Fuentes et al., 2010), and scavenging of
31 surfactants (Zhou et al., 1998). Also, they have an important influence on the optical (Frouin
32 et al., 2001, Stramski, 1994, Stramski and Tegowski, 2001, Zhang et al., 1998) and acoustical
33 (Ainslie, 2005, Terrill and Melville, 2000) properties in the upper ocean. The most important
34 factor in understanding these processes is the distribution of bubble sizes in the top few meters
35 of ocean (Deane and Stokes, 2002) The bubble plumes formed during the first seconds after a
36 wave breaks are characterised by very high void fraction (0.1-10%), rapid changes in bubble
37 size distributions, and a wide range of bubble radii, from a few microns to a few millimetres
38 (Czerski et al., 2011). Consequently, a detailed understanding of the physics requires in situ
39 and precise measurements of bubble populations with adequate temporal and spatial resolution.

40 A high-resolution bubble imaging instrument was designed and successfully deployed in the
41 North Atlantic Ocean. The instrument frame rate was 15 frame/sec and the effective exposure
42 time for each frame was 4 μ s. The image resolution was 2048 \times 2048 pixels and the total
43 recording time for a single deployment was approximately 8.5 hours. Extracting bubble sizes
44 accurately from these images is very important for further data analysis. Oceanographic
45 conditions change slowly over many hours, so any meaningful monitoring of bubble plumes
46 must record data over long time periods while maintaining high time resolution. Therefore, an
47 automated and robust algorithm is required for bubble image analysis.

48 Several algorithms have been developed in the past to analyse bubble images. Some of these
49 algorithms have been used to analyse oceanic images. For instance, Stokes and Deane (Stokes
50 and Deane, 1999) developed an optical instrument to study the bubbles within breaking waves.
51 Their image processing algorithm included two pre-processing operations: correcting non-
52 uniform illumination and thresholding. Correcting the non-uniform illumination involved four
53 steps: morphological operation (closing) to estimate the background illumination, convolution
54 with a 15×15 Gaussian kernel to smooth the image, subtraction of the smoothed image from
55 the original image to remove background illumination variation, and scaling to improve the
56 image contrast. Thresholding was then applied to create a new binary image followed by a
57 Hough transform to detect the bubbles in that binary image. Leifer et al. (Leifer et al., 2003)
58 introduced another instrument for imaging bubbles within breaking waves. They used a
59 thresholding technique to produce binary images. However, this can potentially introduce large
60 errors in the measured bubble size distribution because of the change in the background
61 illumination. Furthermore, the bubbles positioned within the light sheet are much brighter
62 compared to the bubbles outside the sheet. Thomanek et al. (Thomanek et al., 2010)
63 demonstrated an automated gas bubble imaging system to measure bubble sizes at the sea
64 floor. They used a Canny edge detector and the MATLAB function “regionprops” to determine
65 the size and centre of each bubble. In comparison to thresholding, edge detection is more
66 accurate in terms of identifying bubbles in inhomogeneous illuminated areas and analysing
67 images with a gradual decrease in light intensities. However, the main disadvantage of edge
68 detection is the enhancement and shrinking in the bubble boundaries. Zielinski et al. (Zielinski
69 et al., 2010) showed a laboratory set up that consists of frontal illumination and video camera
70 to image bubbles in an aquarium. They used a sequence of optical flow algorithm,
71 thresholding, and region filtering to process the video images. The optical flow analysis was
72 also used by Boelmann and Zielinski (Boelmann and Zielinski, 2015) to identify bubbles in

73 images collected by a remotely operated underwater vehicle in west Svalbard. In the optical
74 flow method, the apparent motion of bubbles in the images can be related to each other as a
75 collection of displacements in the image plane. However, this method is prone to inaccuracies
76 caused by illumination changes, occlusion, and noise (Nixon and Aguado, 2002) . Wang and
77 Socolofsky (Wang and Socolofsky, 2015) developed a stereoscope imaging system for
78 measurement of natural seep bubble size distributions in the Gulf of Mexico. They applied
79 Canny edge detection for low-density bubble images. For high-density bubble images, they
80 used a Sobel gradient mask to obtain a binary image and a watershed transform to perform
81 image segmentation on the overlapping bubbles. However, the watershed transform is sensitive
82 to noise (Honkanen et al., 2005) .

83 On the other hand, a number of algorithms have been developed to analyse bubble images
84 collected from chemical reactors and bioreactors. For instance, Taboada et al. (Taboada et al.,
85 2006) presented a semi-automated image analysis algorithm to count bubble sizes and oil
86 droplets in complex dispersions occurring in bioreactors. Their algorithm consists of two
87 stages: pre-processing to obtain a binary image and post-processing to extract circular bubbles
88 and droplets using the Hough transform. The first pre-processing stage was achieved using
89 commercial imaging software (Image Pro Plus 5.0, Media Cybernetics) and consists of three
90 filtering operations (median, flatten and well filter) and two morphological operations (opening
91 and skeleton). Honkanen et al. (Honkanen et al., 2005) described an experimental setup to
92 image a turbulent flow in a pipe and detect in focus, overlapping, and elliptical bubbles. Three
93 pre-processing steps were carried out according to their recognition algorithm: median filter to
94 remove background noise, image normalization to normalise pixel intensities, and thresholding
95 and grey scale gradients to obtain a binary image. The overlapping elliptical bubbles in this
96 binary image were extracted by examining the perimeter arcs of individual bubbles. This is
97 achieved by calculating the overall perimeter of a segment, finding the connected points at the

98 perimeters of the overlapping objects, grouping the perimeter arcs for the same object, and
99 fitting ellipse to the clustered perimeter arcs of the object. The main disadvantages of their
100 algorithm is it is computationally expensive. Zhong et al. (Zhong et al., 2016) established an
101 experimental setting to image bubbly water in a gas-liquid reactor. Their image analysis
102 method was based on three pre-processing operations (background subtraction, median
103 filtering and thresholding), forming template database of single bubble images, splitting
104 contours for every overlapped bubble, and reconstructing the segmented bubbles. The main
105 drawbacks in this method are that it cannot run autonomously because single bubble images
106 are required for every bubble in the original image and it is very sensitive to the background
107 change in illumination.

108 The algorithms discussed above used pre-processing techniques such as filtering to remove
109 noise and low-level feature extraction approaches such as thresholding and edge detection to
110 extract basic features in the image to speed up the subsequent high-level feature extraction
111 stage (Gonzalez and Woods, 2008, Nixon and Aguado, 2002). However, there are many
112 limitations in the performance of these techniques. The performance of thresholding techniques
113 are limited by the object (bubble) size, contrast, noise, mean difference between the object and
114 the background intensities, and variances of object and background (Lee and Chung, 1990).
115 Noise reduction by filtering operations results in blurred and distorted edges since both noise
116 and edges contain high frequency contents (Liu and Fang, 2015). Traditional edge detector
117 operators such as Sobel, Laplacian, Roberts and Canny are based on gradient methods
118 (Gonzalez and Woods, 2008, Nixon and Aguado, 2002). Therefore, these first order detectors
119 are sensitive to noise (Liu and Fang, 2015). Abdou and Pratt (Abdou and Pratt, 1979)
120 developed a quantitative figure of merit to evaluate the ability of these traditional operators to
121 detect edges as close as possible to the ideal edges. They demonstrated that this figure of merit
122 substantially decreased with reducing the signal-to-noise ratio in the image. Liu and Fang (Liu

123 and Fang, 2015) used the Abdou figure of merit to evaluate applying these traditional edge
124 detector operators on various images with the same noise level. They showed that the
125 performance of these detectors depends significantly on the shape of the objects in these
126 images. Moreover, they found that the detection accuracy decreased to approximately 54% in
127 an image of circular coins. Because of these difficulties any pre-processing must be applied in
128 such a way as to not remove or distort the underlying signal of interest, and the ideal solution is
129 an algorithm that avoids the pre-processing stage entirely.

130 This paper describes a robust automated algorithm for analysing oceanic images based on the
131 Hough transform. The algorithm uses the intensity information in the images directly without
132 any pre-processing stage. The algorithm can extract bubbles over a wide radii range from 1 to
133 25 pixels (approximately 20 to 406 μm) accurately. The paper is organised as follows: a brief
134 description of the imaging instrument is given in section 2; the deployment and measurement
135 in the ocean is illustrated in section 3; section 4 describes the automated bubble extraction
136 algorithm, its implementation and evaluation; section 5 presents bubble size distributions
137 obtained from applying the algorithm on a sequence of images; the discussion of the results is
138 in section 6; and we conclude in section 7.

139 **2. Optical instrument for imaging bubbles**

140 Many acoustical and optical techniques have been developed to measure bubble size
141 distributions in the laboratory and open sea. The acoustical techniques (Farmer et al., 1993,
142 Medwin, 1970, Medwin, 1977) are sensitive to bubble radii from 1-500 μm and low void
143 fraction whilst optical techniques (Geißler and Jähne, 1995, Jähne and Geißler, 1994, Leifer et
144 al., 2003, Wang and Monahan, 1994) can be used to measure bubble distributions at low and
145 high void fraction and over a wide radii range from 20 μm -5 mm.

146 This section provides a brief description of the bubble imaging instrument that we designed to
147 capture high quality images and increase the measured bubble size range. More details about
148 the design considerations and hardware components can be found in Al-Lashi *et al* (Al-Lashi et
149 al., 2016). The camera and its control electronics were housed in a waterproof pressure case
150 (see figure.1). Strobe lighting illuminated a thin slice of water approximately 4cm x 4 cm x 5
151 mm, and this sample volume was positioned a few centimetres in front of the camera housing.

152 The hardware components of the bubble imaging system can be divided into six modules: the
153 power management board to supply the necessary power to the components, the strobe system
154 to form the light sheet, the machine vision camera, the single board computer which controls
155 the camera and saves the images on the solid-state drive, and the waterproof enclosure to
156 protect the electronic modules. The principle operation of the instrument is based on the
157 formation of a light sheet in front of an optical Perspex window. Images are formed by
158 focusing the scattered light caused by the bubbles inside the lightsheet through a mega-pixel
159 telecentric lens mounted on a high resolution CCD camera.

160 The hardware components were mounted in a waterproof housing that is divided into three
161 chambers separated by two steel disks as shown in figure 1. The top chamber contains the
162 single board assembly with the main electronics, the middle chamber contains the camera
163 assembly with the imaging components, and the bottom chamber contains the strobe assembly
164 with the illumination components. The mirror assembly was fixed outside the housing to form
165 the light sheet in front of camera optical window.

166 **3. Deployments and measurements in the open sea**

167 The bubble imaging instrument in its autonomous configuration was deployed seven times in
168 the North Atlantic Ocean in 2013 (including buoyancy and instrument configuration trials) and
169 deployment lengths ranged from a few hours to five days. These deployments were part of the

170 HiWINGS campaign to study air-sea gas exchange during storms. As part of this campaign, a
171 suite of bubble measurement instruments was mounted on a large free-floating buoy. The
172 average hourly wind speed during the deployments ranged from 10 m/s to 30 m/s, and the
173 significant wave height varied from one to ten metres. Figure 2 shows the bubble instrument
174 mounted on the free-drifting spar buoy, as the buoy is being deployed. The camera was
175 positioned approximately 2 m below the ocean surface when the buoy was floating upright.
176 The design and performance of the spar buoy was well described in (Pascal et al., 2011).
177 Whitecaps (the patches of foam left at the surface after the passage of a breaking wave) were
178 imaged by another camera system positioned above the water surface. To synchronise both
179 instruments, the power supplied to them was controlled by two timers, which were
180 programmed at preset intervals. The total number of captured images during seven times
181 deployments was approximately 850000.

182 Depending on the bubble shapes and the activities in the ocean, the captured images can be
183 classified into 3 main categories: large bubble, small bubble, and complex images. The vast
184 majority of these captured images contain small bubbles. The number of complex and big
185 bubble images in the seven deployments were 5 and 269, respectively. These images are
186 classified automatically by the algorithm as illustrated in the implementation section 4a.

187 The air bubbles in the light sheet appear as bright circular objects in the images. The bubble
188 shape depends on the surface tension which dominates the shape as a bubble gets smaller.
189 Therefore, small bubbles tends to be spherical whilst large bubbles are more likely non-
190 spherical (Leighton, 1994). More complex bubble shapes can be described mathematically
191 using spherical harmonics (Leighton, 1994). Figure 3 shows a sample of the captured images
192 during deployment in the North Atlantic Ocean. The big bubbles are mainly non-spherical in
193 (a) whilst the small bubbles are circular in (b). Moreover, the small bubbles that are not located

194 in the light sheet appear as disks. Some of the small bubble images also contain marine
195 creatures such as a copepod as shown in (c).

196 Complex images contain bubble features that are not extracted by the automated algorithm
197 described in this paper. We choose to implement a simpler algorithm that avoids processing
198 complex images since the number of these images is significantly small (5 images only).
199 However, bubbles in these images can still provide valuable information. For instance, the
200 bubble plume shown in (d) could provide useful information about bubble formation
201 mechanisms (Deane and Stokes, 1999).

202 **4. Automated bubbles extraction algorithm**

203 Bubbles in the image appear as high intensity rings or disks as shown in figure 4. The
204 intensities of the bubble wall pixels are higher than the surrounding pixels in the image
205 background and can be used by an algorithm to automatically locate and extract the position
206 and size of the bubbles. There are a number of possible algorithms that could be used for the
207 extraction. These range from model-based approaches to deformable approaches that can
208 accommodate large variations in shape characteristics. Here, we are primarily interested in
209 extracting bubbles in the size range 20-500 μm and these are spherical to a good approximation
210 due to surface tension. Hence, a model-based approach using the Hough transform is chosen
211 for its robustness.

212 *a. Hough transform for circular shapes*

213 The Hough transform (Hough, 1962) is a high-level feature extraction technique based on
214 shape matching (Nixon and Aguado, 2002). In particular, it is widely used to extract lines
215 (Duda and Hart, 1972), circles (Kimme et al., 1975), and arbitrary shapes (Ballard, 1981) from
216 images. The technique is based on an evidence gathering approach where votes are cast in an

217 accumulator array, which is parameterised according to the model of the shape to be extracted,
 218 and can be shown to be an optimal form of template matching.

219 The Hough transform operates on the principle that candidate edge points have high intensities.
 220 In practice this means that an edge detector is often required as a pre-processing stage to
 221 transform object boundaries (Ballard, 1981, Deane and Stokes, 1999, Kimme et al., 1975,
 222 Zheng et al., 2004). However, due to the formation of the images from the bubble camera it is
 223 possible to avoid this step as the edges are already in this form. This is advantageous because
 224 the gradient-based edge operators can amplify noise as well as skewing peaks off centre in the
 225 accumulator (Gonzalez and Woods, 2008, Nixon and Aguado, 2002).

226 1) ACCUMULATOR SPACE

227 The equation of circle is given by

$$228 (x - x_0)^2 + (y - y_0)^2 = r^2 \quad (1)$$

229 where the point (x_0, y_0) represents the circle centre, points (x, y) correspond to the circle locus,
 230 and r represents the circle radius. A bright pixel in the image is a candidate for a point on the
 231 locus of a number of possible circles. The algorithm votes by incrementing the accumulator for
 232 those values of the parameters (x_0, y_0, r) that satisfy eq. 1 given the pixel co-ordinates (x, y) .
 233 This corresponds to a cone in the three dimensional accumulator space parameterised by $(x_0, y_0,$
 234 $r)$. The votes from all sets of edge points of a circle in the image will pass through the same
 235 point in the accumulator space. Thus, this point has the maximum vote (peak) in the
 236 accumulator space and can be used to extract circle parameters. Since higher intensities
 237 indicate greater confidence in edge points this can be used to weight the vote in the
 238 accumulator space,

$$239 A(x_0, y_0, r) += g(x, y) \quad (2)$$

240 where A is the accumulator value at the coordinates (x_0, y_0, r) and g is the pixel intensity at
 241 coordinates (x, y) . For each value of r , the accumulator coordinates (x_0, y_0) are calculated using
 242 the parametric form of eq. 1,

$$243 \quad x_0 = x - r \cos \theta, \quad y_0 = y - r \sin \theta, \quad (3)$$

244 where $\theta \in [0, 2\pi)$. The spatial resolution of the coordinates (x, y, r) in the accumulator space is
 245 1 pixel, and θ is quantised to one degree.

246 2) PEAK DETECTION

247 Promising circles are indicated by large values in the accumulator array. In order to avoid
 248 multiple circles being detected where only one exists in the image it is necessary to do peak
 249 detection. The accumulator array is searched for local maxima by selecting the accumulator
 250 cells that have higher votes than their 3×3 spatial neighbourhood. However, there are many
 251 additional peaks in the accumulator array that are not relevant to the circular bubbles. For
 252 instance, peaks may be created by: the surrounding bubble walls, the bubble walls and
 253 background, and the marine creatures. These are similar to the bubble peaks. Moreover, the
 254 bubble wall can generate many peaks due to its thickness. Figure 4 shows extracted circles in
 255 an image that corresponds to these redundant peaks. Thus, it is very important to filter out
 256 these unwanted peaks.

257 The peak filtering can be divided into six stages: radial distribution (RD), suppressing wall
 258 thickness peaks, filtering surrounding bubble walls or walls-background peaks, filtering edge
 259 peaks, and filtering copepod peaks. The *radius distribution*, denoted RD , measures the
 260 homogenous distribution of the pixel intensities around the bubble centre in the image space. It
 261 can be expressed as

$$262 \quad RD = \frac{\left| \int_{\theta=0}^{2\pi} e^{i\theta} g(x,y) d\theta \right|}{\int_{\theta=0}^{2\pi} g(x,y) d\theta} \quad (4)$$

263 The pixel coordinates (x, y) are calculated using eq.2 for each candidate peak in the
 264 accumulator space. To implement this measure, the RD value calculated in eq.4 needs to be
 265 compared with an absolute value. It is found by the evaluation on a number of images that the
 266 RD values for the bubble peaks are less than 0.4.

267 The RD is very efficient in removing the peaks between the bubble walls and background. In a
 268 highly dense bubble image, approximately 60% to 75% of the unwanted peaks are removed by
 269 the RD measure. Nevertheless it is not effective in filtering the wall thickness, and surrounding
 270 walls peaks. Before proceeding to the next refining stages, the peaks in the candidate list are
 271 sorted in descending order according to their accumulator votes and radii. Consequently, the
 272 larger circles are selected first from the list in the next stages. It was decided to follow this
 273 hierarchical approach that concentrates first on the larger circles because many false smaller
 274 circles exist inside the bubble, on the bubble wall and between the bubble wall and the
 275 background. The wall thickness peaks can be identified by comparing the distance between
 276 each candidate peak with all the peaks in the accumulator array. The distance between two
 277 circles with peak coordinates (x_1, y_1, r_1) and (x_2, y_2, r_2) can be calculated using the following
 278 formula

$$279 \quad \delta = \sqrt{(x_1 - x_2)^2 + (y_1 - y_2)^2} - (r_1 + r_2) \quad (5)$$

280 where δ is positive if the circles do not overlap and measures the minimum distance between
 281 the circle loci. Eq.5 was used to remove the entire set of overlapping peaks that belong to a
 282 particular bubble. This set of overlapping peaks includes the wall thickness peaks as well as the
 283 small circle peaks on the bubble wall and between the bubble wall and background. These
 284 redundant peaks are removed from the candidate list by following the hierarchical approach
 285 mentioned in the previous paragraph. The larger peaks are first selected from the candidate list.
 286 Then their distances are compared with the smaller peaks in the list using eq.5. It was found by

287 evaluation on a number of images that $\delta \leq 1$ is adequate to detect the entire set of smaller peaks
288 that overlap with the bubble peak. Consequently, these overlapping peaks are removed from
289 the list.

290 The surrounding wall peaks are generated by the walls of adjacent bubbles. It is observed that
291 some parts of the background are covered by the surrounding wall circles in the image space.
292 Therefore, the detection of the surrounding wall peaks is based on counting the number of
293 pixels at the circumference in the image space that have intensities less than double the
294 background intensity.

295 Even though copepods are not circular many connected circles are generated inside the
296 copepod bodies due to their high pixel intensities. The copepod and bubble peaks in the
297 accumulator space can be very similar and therefore it is challenging to distinguish between
298 them. Two criteria have been used to identify the copepod peaks. These are the peak value in
299 the accumulator space and the distance between this peak and their neighbours. The copepod
300 peak is the one with highest vote and has a close distance with at least three neighbouring
301 peaks. If these two conditions are satisfied, then the distance between the connected circles in
302 this region are evaluated using eq.5. The algorithm continues evaluating the distance between
303 each new detected copepod circle and its neighbours when satisfying the value of δ in eq.5.
304 Two types of images were analysed to select the right value of δ . The first type of image
305 contains copepods with different shapes and sizes whilst the second type contains only
306 bubbles. It was found that $\delta \leq 12$ in eq.5 is adequate to detect the entire set of peaks that belong
307 to a particular copepod. Moreover, it would not detect the bubbles in the free copepod images.
308 These copepod peaks are removed from the candidate list.

309 The bubbles that are close to the image edges appear as incomplete circles. Therefore, it is not
310 possible to extract them with the same accuracy. The peaks of these incomplete bubbles are
311 excluded from the candidate list by testing how close their coordinates are from the edge of the

312 accumulator array, and the reduction in effective field of view for large bubbles can be
313 compensated appropriately in any final histogram calculation.

314 3) CLASSIFICATION

315 After refining the unwanted peaks, the remaining peaks in the accumulator space are classified
316 into two categories: rings (bright rings around dark centre) and disks (filled circles). The
317 illumination around the ring bubble wall varies because the light source does not illuminate the
318 light sheet evenly from all directions, but has an increased intensity around the centres of the
319 mirrors creating the light sheet. As a consequence, the ring bubbles appear as four dots for the
320 smallest resolvable bubbles in the image space as shown in figure.4.

321 The coordinates and radii of the ring and disk bubbles are successfully detected by the
322 hierarchical approach of radii extraction that was described in the previous section (section
323 A.2). However, the bubble rings have a more precise bubble radii distribution than the disks.
324 This is because the circular bubble rings are in the light sheet (in focus) and are very well
325 identified. The ring centre intensity is close to the background intensity and lower than its
326 circumference intensities. In contrast, the filled disks (out of focus) are not in the light sheet
327 and the pixel intensities are irregularly distributed around their centres. Therefore, these out of
328 focus bubbles are excluded from the bubble size distribution calculations.

329 The classification into rings and disks is achieved by comparing the average intensity of the
330 central bubble region with that of its periphery.

331 4) IMPLEMENTATION

332 To implement eqs.1 to 3, it is necessary to specify the size and resolution of the accumulator.
333 To speed up the image analysis, the maximum bubble radius needs to be known before running
334 the algorithm. To find this radius, the average intensity of each single image in two major
335 deployments (8.5 hours each) was calculated. It was found that the maximum bubble radii in

336 high intensity images did not exceed 20 pixels (approximately 400 μm). Therefore, the radii
 337 range used in the algorithm is from 1 to 25 pixels (approximately 20 to 406 μm). The
 338 accumulator coordinates (x_0, y_0) have the same range as the image space (2048×2048) and the
 339 resolution for the coordinates (x_0, y_0) and r is 1 pixel.

340 The implementation of the algorithm can be summarised as follow:

- 341 a) Calculate the image histogram to assess the image type (small bubbles, big bubbles or
 342 complex image). This is accomplished by examining the number of pixels at a
 343 particular grey level in the image histogram. The algorithm continues running next
 344 steps (b to k) only if the image contains small bubbles.
- 345 b) Build the 3-dimensional accumulator array $A(x_0, y_0, r)$ using the voting scheme in eq.2.
 346 For each value of r , there are 2048 rows and 2048 columns of the accumulator
 347 coordinates (x_0, y_0) . This array can be built by varying the coordinates of circle locus
 348 (x, y) in eq.3 from 0 to 2047 for a particular value of r . The value of θ in eq.3 is varied
 349 from 0 to 2π for a given circle locus (x, y) . The vote of the accumulator array $A(x_0, y_0, r)$
 350 in eq.2 is incremented only for the coordinates (x_0, y_0) that lie within the image
 351 dimension.
- 352 c) Find the peaks in the accumulator array by selecting the accumulator cells that have
 353 higher votes than their 3×3 spatial neighbourhood. This can be accomplished by
 354 comparing the vote of each accumulator cell $A(x_0, y_0, r)$ with its neighbours. A list of
 355 peaks is created in this step. This list contains the accumulator votes and coordinates
 356 that have larger votes than its neighbourhood.
- 357 d) Refine the peaks list using the radial distribution measure in eq.4. The circle loci for
 358 each accumulator coordinate (x_0, y_0, r) in the list of peaks are calculated by varying θ in
 359 eq.3 from 0 to 2π . The intensity values of these locus coordinates in the image space are

360 summed to calculate the RD in eq.4. The accumulator vote and coordinate for a given
 361 peak is removed from the list if the RD value is larger than 0.4.

362 e) Sort the peaks in descending order according to their radii and votes so that priority is
 363 given to the larger bubbles as shown in section a.2. This can be done by calculating the
 364 product of accumulator vote and radius of each peak and comparing its values with all
 365 the peaks in the list.

366 f) Refine the list by removing the surrounding walls and wall-background peaks. The
 367 circle loci for each accumulator coordinate (x_0, y_0, r) in the list of peaks are calculated by
 368 varying θ in eq.3 from 0 to 2π . A counter is created and incremented by 1 if the
 369 intensity value for a given locus coordinate in the image space is less than double of the
 370 background intensity. The peak is discarded from the list if the counter value is larger
 371 than 180.

372 g) Refine the list by removing the wall thickness peaks using eq.5. The distance between
 373 peak coordinates (x_1, y_1, r_1) and (x_2, y_2, r_2) in the list are calculated and the peaks of
 374 smaller circles (lower votes) are removed from the list if $(x_1-x_2)^2+(y_1-y_2)^2 \leq (r_1+r_2+1)^2$.

375 h) Refine the list by removing the peaks at the edges. For a given accumulator coordinate
 376 (x_0, y_0, r) , its peak is discarded if $(x_0-r) < 0$ or $(x_0+r) > 2048$ or $(y_0-r) < 0$ or $(y_0+r) > 2048$.

377 i) Refine the list by removing the peaks caused by copepods. The distance between the
 378 coordinate with highest vote peak (x_1, y_1, r_1) and other peak coordinates (x_2, y_2, r_2) in
 379 the list are calculated using eq.5. A counter is created and incremented by 1 if $(x_1-x_2)^2+$
 380 $(y_1-y_2)^2 \leq (r_1+r_2+12)^2$. The highest vote peak and its neighbours will be regarded as
 381 copepod peaks if the counter value is equal or larger than 3. In this case, the algorithm
 382 continues evaluating the distance between theses detected copepod peaks and its
 383 neighbours. The neighbourhood peaks will also be discarded from the list if $(x_1-x_2)^2+$
 384 $(y_1-y_2)^2 \leq (r_1+r_2+12)^2$.

- 385 j) Classify the peaks as rings or disks. For a given accumulator coordinate (x_0, y_0) in the
 386 list, the locus coordinates of two circles with radii r and $0.1r$ are calculated by varying θ
 387 in eq.3 from 0 to 2π . The average intensities of these two circle loci in the image space
 388 are calculated and compared with the circle centre intensity.
- 389 k) Calculate the histogram of the bubble rings and disks, and save them in two different
 390 files.
- 391 l) Load the next image in the directory and repeat steps a to k.

392 Steps b to j are explained in more details in section A.2.

393 *b. Evaluation*

394 To demonstrate the performance, the Hough Transform was evaluated using synthetic and real
 395 images. To simulate the bubble images the following model was used to generate bubbles,

$$396 \quad psf = 255 \left(1 - \frac{dist}{spd}\right) \left(\frac{1}{2} + \frac{r}{2 rmax} \cos\left(4 \tan^{-1} \frac{y}{x}\right)\right) \quad (6)$$

397 where psf is the point spread function that describes the blurring around a particular circle
 398 locus(x,y), spd represents the blurring of the bubble wall, $dist$ represents the distance between
 399 the circular bubble locus(x,y) and its centre, r represents the bubble radius, $rmax$ represents the
 400 maximum radius in the synthetic image, and the cosine expression simulates the variation in
 401 illumination around the bubble due to the non-uniformity of the four light sources forming the
 402 light sheet; the inverse tangent is computed using atan2 to retain sign information. The spd
 403 value in eq.6 was gradually increased from 1 to 6 to expand the blurring of the bubble walls
 404 and reduce the distance between them. Moreover, the bubble radii were in the range 1 to 50
 405 pixels and randomly positioned in the images. The resolution of these images was 2048×2048
 406 pixels and the number of bubbles was between 400 and 700. The total number of synthetic
 407 images was 60 where 10 images were tested for each spread value. The absolute errors in the
 408 coordinate $\epsilon_{x,y}$ and radius ϵ_r , are calculated as follows

$$409 \quad \epsilon_{x,y} = |D_{x,y} - T_{x,y}| \quad (7)$$

$$\epsilon_r = |D_r - T_r|$$

410 where D and T stand for the detected and true circle, respectively.

411 Table.1 shows the maximum and the average errors in the coordinates and radii obtained from
 412 increasing the spd value from 1 to 6. It can be seen that there is a gradual increase in the
 413 maximum and average errors when this value exceeds 2. In addition, the average errors in the
 414 radii are much greater than the coordinates. It has been found that the majority of these radii
 415 errors result from bubbles with radii smaller than 3 pixels and the absolute error in the radius is
 416 ± 1 pixel. This is because the shapes of these small bubbles change from rings to disks in
 417 response to the increase in the spd value. Figure.5 shows the effect of increasing the spd value
 418 from 1 to 6 on the bubble shapes and distance between them. It is clear that the pixel
 419 intensities forming the bubble walls are varied substantially and significant numbers of the
 420 bubbles are overlapping when the spread is 6. However, the algorithm correctly extracts these
 421 overlapped bubbles as shown in (d). In addition, (d) shows that the algorithm does not detect
 422 the incomplete bubbles at the image edge.

423 80 real images were selected to evaluate the algorithm. The selected images contain large
 424 numbers of ring and disk bubbles and copepods as shown in figure.6. It can be seen that the
 425 algorithm extracts the majority of the ring and disk bubbles in these images without counting
 426 the copepod.

427 **5. Bubble size distributions**

428 The bubble extraction algorithm was applied to the entire sequence of images collected in two
 429 main deployments of the bubble imaging instrument. The bubble imaging instrument was
 430 configured to capture images for 40 minutes every 3 hours. The total number of processed
 431 images was approximately 850000. Figure.7 shows a sample of the data collected during

432 deployment in the North Atlantic Ocean on 25th October 2013. The wind speed was 26 m/s.
433 The void fraction versus time of recording is shown in (a). The one second averages were
434 calculated based on the 15 sequential frames taken in that one second, and this average was
435 calculated for every second throughout the 40 minute measurement period. A subsection
436 identified by vertical dashed line in (a) is plotted in more detail in (b). The circle (16:18:33),
437 diamond (16:19:45), and triangle (16:19:51) in (b) are the markers for the three bubble size
438 distributions plotted in detail in (c). Each distribution was scaled by the measured volume of
439 water which was approximately $4.0 \times 4.0 \times 0.5 \text{ cm}^3$. The bubble numbers quoted here are the
440 bubble number per micron radius increment per unit volume, which is the conventional unit
441 used in the oceanography literature. Each size distribution shown is also a one second average,
442 and the total number of bubbles counted to calculate each one-second size distribution was 28
443 (circles), 542 (diamonds) and 1225 (triangles).

444 **6. Discussion**

445 The focus of this paper was the automated extraction of bubble images using Hough transform
446 as the basis. Most of the methods based on the Hough transform for circular shape detection
447 use gradient information which is obtained from applying a first order edge detector to the
448 original image. Therefore, the success of these methods significantly depends on accurate
449 estimates of the edge information. In our approach the pixel intensities are directly used to
450 build the accumulator array for the voting scheme. This was followed by several stages of
451 filtering and a hierarchical radial extraction approach to remove unwanted peaks. This
452 improves the detection accuracy of the Hough transform by approximately 50% (Liu and Fang,
453 2015).

454 The proposed Hough transform has been shown to be successful in extracting bubbles in the
455 synthetic and real images as mention in section IV.3. The test images contain a large number of

456 ring and disk bubbles that overlap in some cases. In addition, the size of the bubble radii was
457 between 1 and 50 pixels (approximately 20 to 1000 μm). The unwanted peaks caused by the
458 overlapping bubbles have been effectively removed by the hierarchical radial extraction
459 approach that first emphasises on the larger particles. Consequently, this hierarchical approach
460 gives a bias to detect larger bubbles. However, this bias can be corrected and included as error
461 bars on the bubble size distributions. The accuracy of extracting ring bubbles is much higher
462 than the corresponding disk bubbles. This is because the bubbles in the light sheet are in focus
463 and seen as a white ring surrounding dark centres. Nevertheless, the unfocused bubbles are
464 observed as disks with irregular distribution of pixel intensities around the centre. Therefore,
465 the histograms of the disk bubbles were saved in another file to separate them from the ring
466 bubbles.

467 The entire image sequence for two major deployments was analysed and a sample of the
468 bubble size distributions measured during an 18 second period are shown in figure 7. There is
469 significant change in the bubble numbers during these short periods. This is likely due to a
470 combination of highly inhomogeneous bubble plumes, and the advection of the bubbles past
471 the optical instrument. In general, the number of bubbles is significantly lower when their sizes
472 exceed 100 microns. Moreover, the smallest extracted bubbles were approximately 20 μm in
473 radius which is equivalent to the Rayleigh resolution limit for such types of oceanic bubble
474 imaging instruments (Deane and Stokes, 1999, Walsh and Mulhearn, 1987).

475 The required computation time and memory for the Hough Transform depends on total number
476 and size of bubbles in the image, the discrete resolution of the accumulator parameters (radii
477 and centres) and the possible range of these parameters. The proposed algorithm was coded in
478 C++ and used OpenCv library for computational efficiency (Bradski and Kaehler, 2008). The
479 C++ program requires approximately 5 seconds to extract one frame on a 2.5 GHz Core i5 Mac

480 laptop with 4GB system memory. It is mainly steps (b) and (c) of implementation (feature
481 extraction stage) that are time consuming.

482 Although the proposed Hough Transform is very robust to extract and count the bubbles, the
483 algorithm's accuracy significantly decreases in particular images. For instance, the bubbles can
484 be large and non spherical, or tightly packed and highly illuminated as shown in figures 3a and
485 3d. Bubbles with radii greater than approximately 1 mm are likely to show a significant
486 distortion from a spherical shape. An advanced approach based on a combination of machine
487 learning and Hough Transform may be required to process such complex images.

488 The proposed algorithm in this paper can be extended to extract elliptical bubbles. This can be
489 done by defining five parameters that represent an ellipse, instead of three parameters that
490 represent a circle. As a result, the algorithm becomes more complicated and slower since it
491 requires significantly greater computational recourses. The complex and elliptical big bubble
492 images were detected and not processed by inspecting their image histograms as illustrated in
493 the implementation section (section 4a.4). The percentage of these images was less than
494 approximately 0.04%.

495 **7. Conclusions**

496 We have presented an automated algorithm for bubble extraction based on the Hough
497 Transform. The algorithm effectively resolves bubbles with a radius of one pixel and
498 discriminates between bubbles and copepods. It was applied to analyse approximately 850000
499 captured images from the ocean.

500 The main novelty of this automated algorithm is that it extracts the bubbles from the original
501 image by using the pixel intensities directly without applying any pre-processing operations.
502 Therefore, the algorithm is less sensitive to noise because it does not use any first order edge
503 operators. In addition, it is not susceptible to the background changes in illumination and

504 effectively extracts bubble sizes as small as 1 pixel in radius. This is because it avoids using
505 any pre-filtering and thresholding operations. The implementation of this automated algorithm
506 is significantly simpler than the ones published in literature and it has been applied to process
507 850000 real ocean images. In addition, we have found that this algorithm performs well for
508 realistic ocean bubble distributions and removing copepods. Real data from the ocean was used
509 to refine the algorithm, in contrast to other methods which are calibrated solely using lab data
510 collected in controlled conditions.

511 We believe that the proposed algorithm can be used to extract circular bubbles in many other
512 engineering, medical and chemical applications.

513 *Acknowledgments*

514 This work was supported by the UK's Natural Environment Research Council (grant
515 NE/J020893/1). The authors would like to thanks the scientists, officers and crews of R/V
516 Knorr who took part in the HiWINGS campaign for their help during deployment of bubble
517 imaging instrument in the North Atlantic Ocean.

518

519

520

521

522

523

524

525

526 **Tables**

527 TABLE 1. Comparison between the errors in the coordinate $\epsilon_{x,y}$ and radius ϵ_r using different
 528 *spd* value (blurring) in eq.6.

Spread (pixels)	Maximum $\epsilon_{x,y}$	Maximum ϵ_r	$\epsilon_{x,y}$ percentage in 10 images (%)	ϵ_r percentage in 10 images (%)
1	0	0	0	0
2	0	0	0	0
3	2	1	0.3	15
4	8	7	1.17	16.1
5	8	8	2.52	14.53
6	9	9	4.99	25.48

529

530

531

532

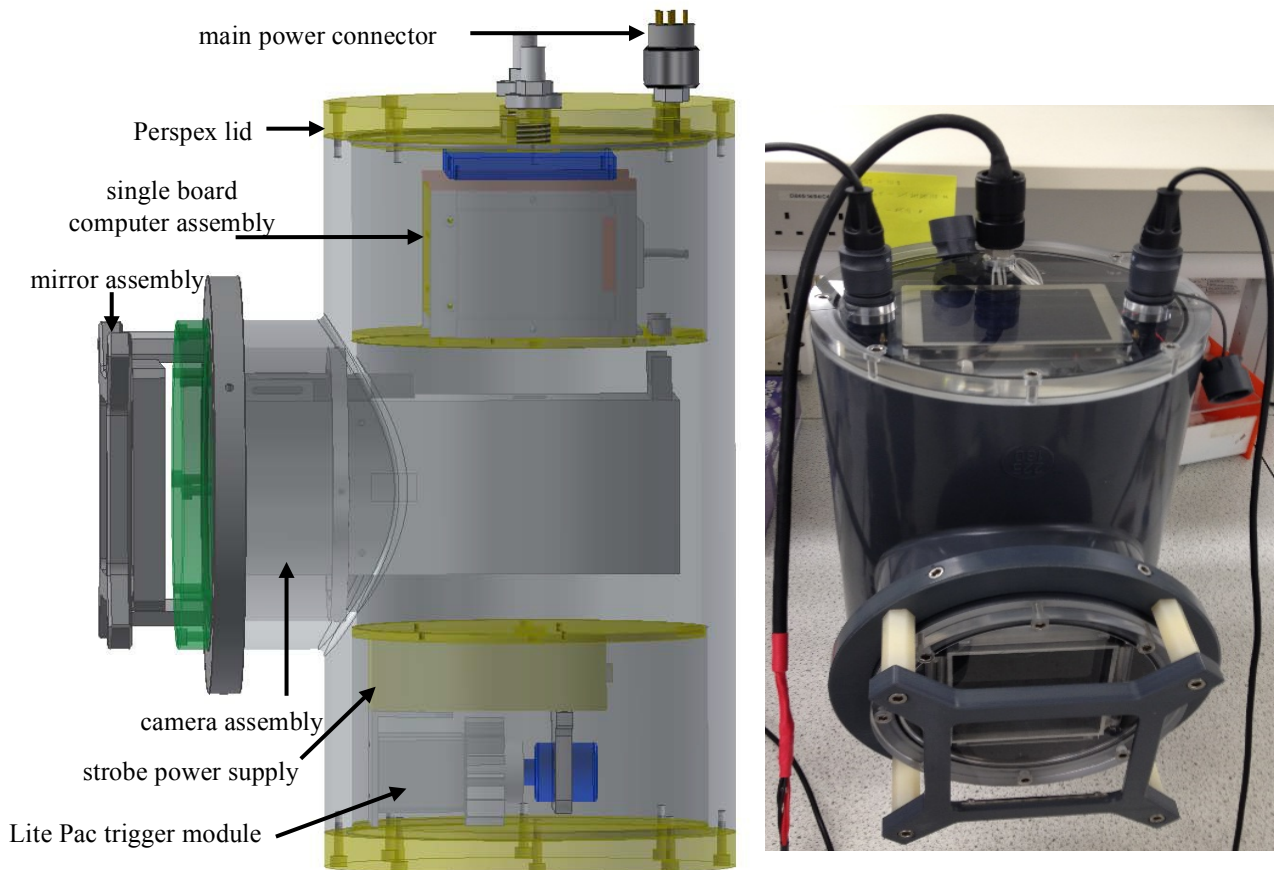
533

534

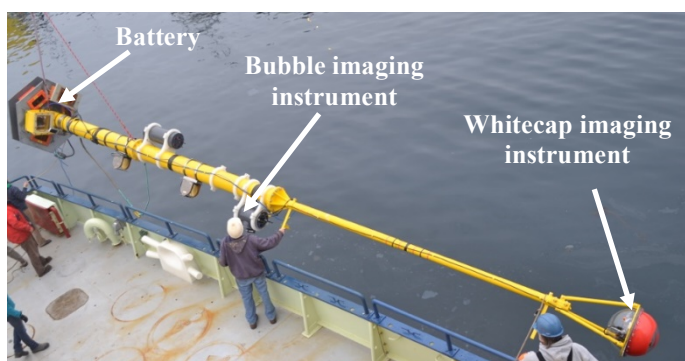
535

536

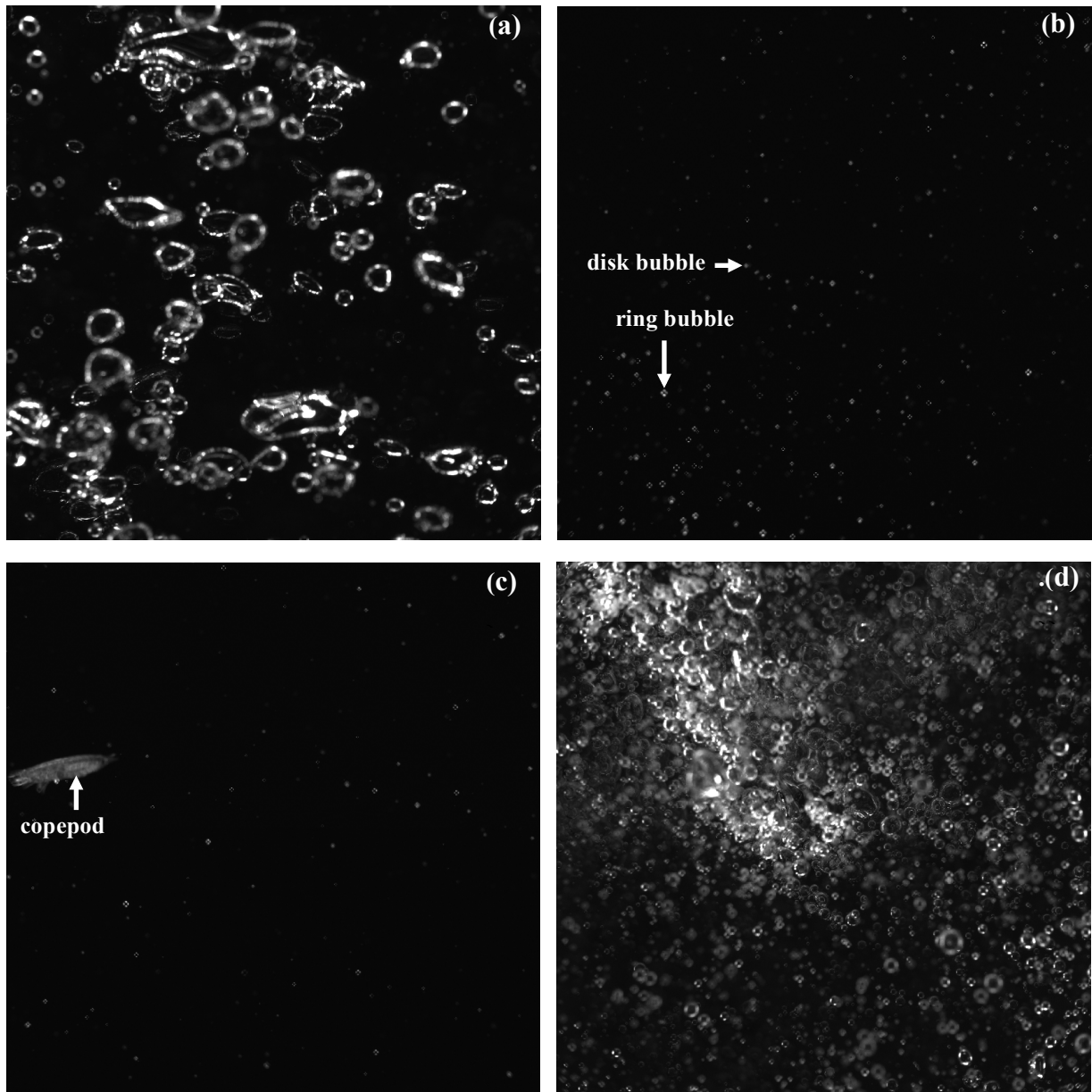
537 **Figures**



538
 539 FIG.1. A cross-section through the instrument housing, showing the layout of the hardware
 540 components (left). The bubble optical imaging instrument and its housing (right). The case
 541 diameter is 225mm \times 160mm, and its length is 407mm.



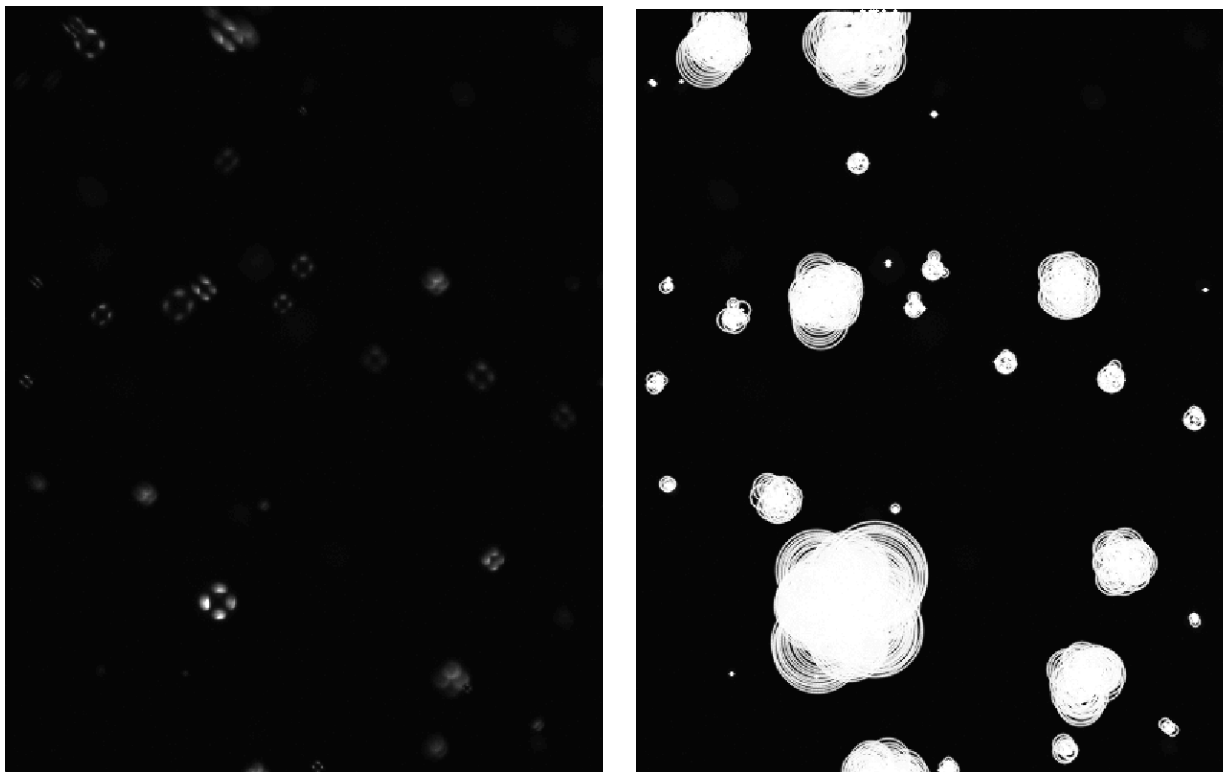
542
 543 FIG.2. The bubble imaging instrument discussed here attached to a spar buoy during
 544 deployment in the sea. The spar buoy length is 11 m. The automated algorithm described in
 545 this paper was used to analyse the images collected by the bubble imaging instrument while it
 546 was mounted in this configuration.



547

548

549 FIG.3. Sample of the images captured during deployment in the North Atlantic Ocean. The
 550 dimensions of these images are $4\text{cm} \times 4\text{cm}$. Image (a) contains non-spherical bubbles. Images
 551 (b) and (c) show two types of circular bubbles: rings and disks. The ring bubble appears as a
 552 bright ring (high intensity) around a dark centre (low intensity) whilst the disk bubble appears
 553 as a filled circle. A copepod was imaged in (c). Image (d) shows a complex image that contains
 554 a bubble plume.



555

556 FIG.4. Hough transform feature extraction without peak filtering. (a) shows a slice in origin image that contains
557 ring and disk bubbles. The extracted circles are highlighted with white colour in (b). There are significant numbers
558 of extracted circles that are not related to the oceanic bubbles. The peaks in the accumulator space that correspond
559 to these extra circles are due to bubble wall thickness and bubble wall background.

560

561

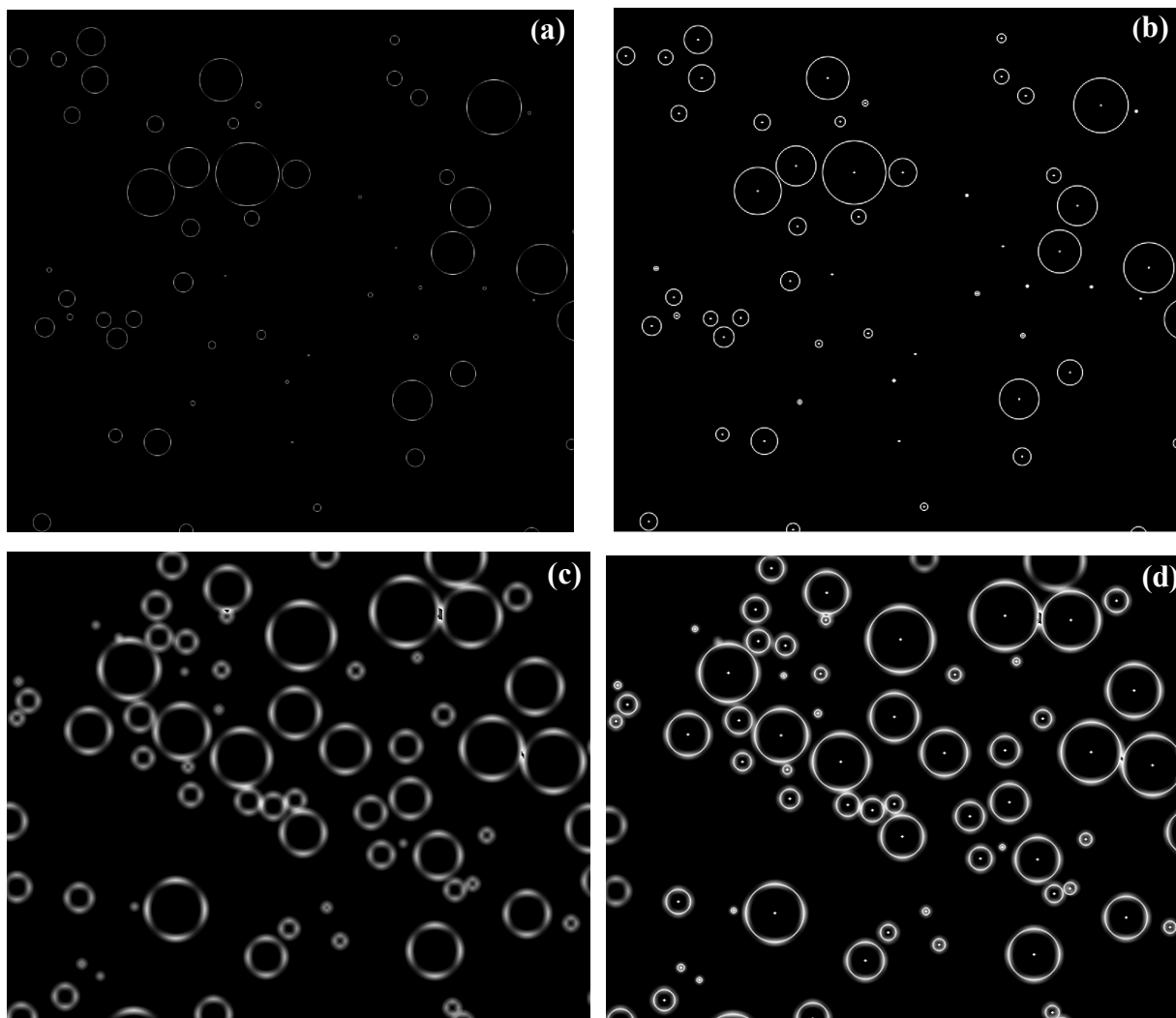
562

563

564

565

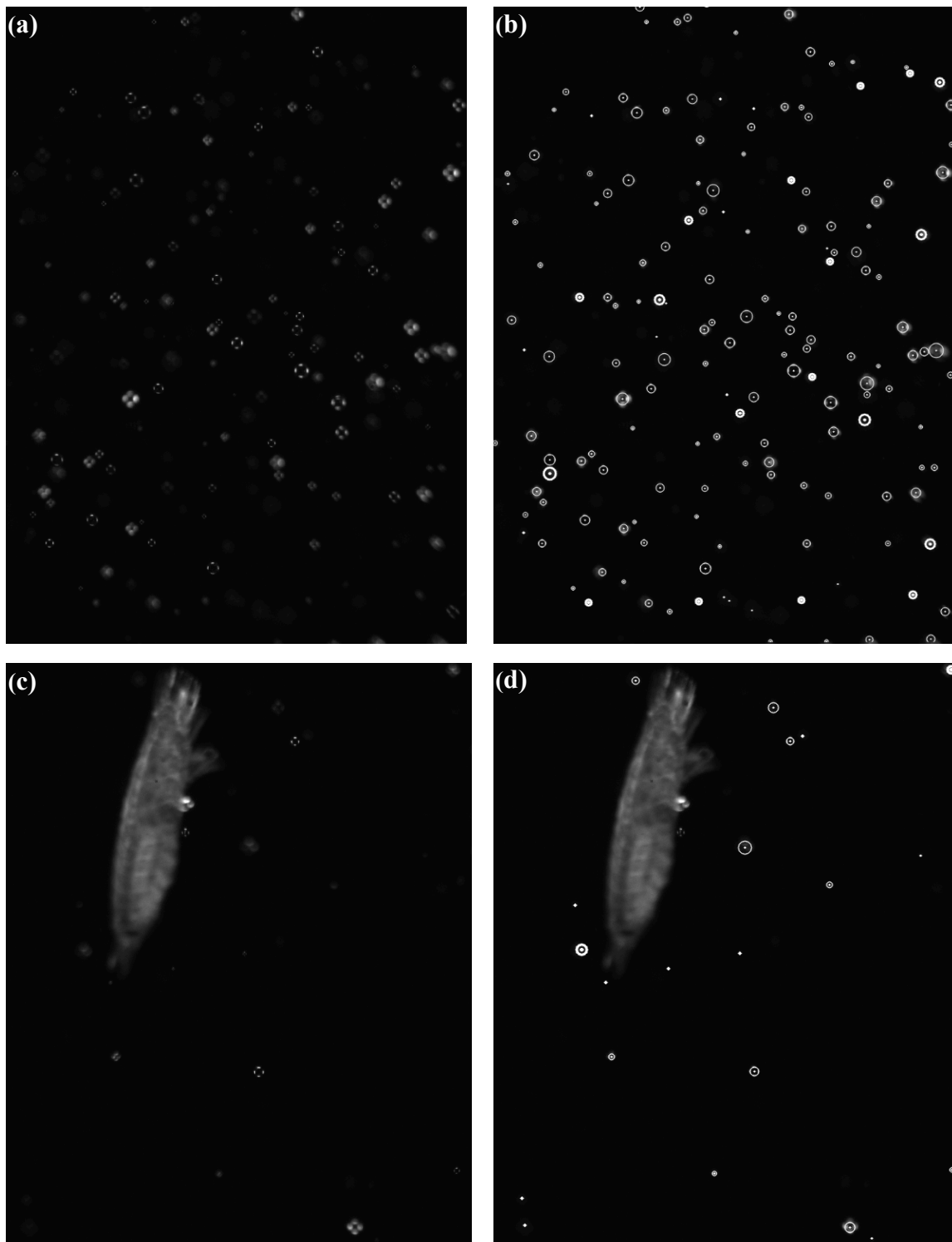
566



567

568

569 FIG.5. Sub regions of the synthetic images to illustrate the change in spread values in table.1.
 570 The spread values are equal to 1 in (a). (b) shows the extracted bubbles in (a). The extracted
 571 bubbles are highlighted with white dot at the centre and white circumference line. The spread
 572 value is equal to 6 in (c). (d) shows the detected bubbles in (c). This region is taken from the
 573 top of an image and therefore, the incomplete bubbles at the edges are not extracted.

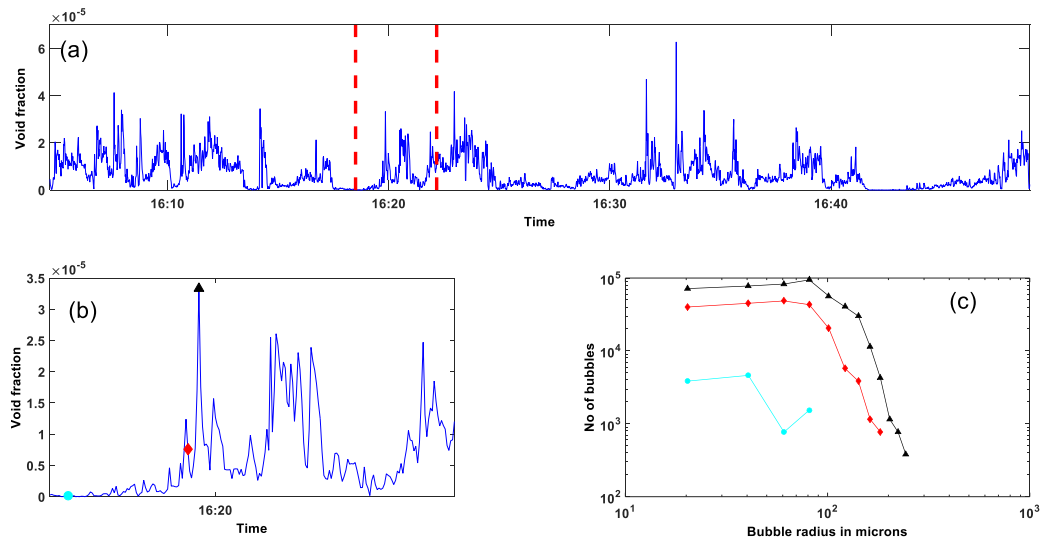


574

575

576 FIG.6. Sub regions of the real images illustrating the algorithm extraction accuracy. Ring and
 577 disk bubbles are shown in (a). (b) shows extracted ring and disk bubbles in (a).The extracted
 578 bubbles are highlighted with white dot at the centre and white circumference line. Brighter
 579 white colour was used to identify disk bubbles. An image that contains a copepod as well as

580 disk and ring bubbles is shown in (c). (d) shows the extracted bubbles in (c), successfully
 581 avoiding false detection associated with the copepod.



582
 583 FIG.7. Sample of the data processed by the bubble extraction algorithm. The top plot shows
 584 the void fraction with time for one 45 minute measurement period. The lower two plots show
 585 an enlarged section of the void fraction plot and the detailed bubble size distributions at the
 586 three marked times.

587

588

589

590

591

592 REFERENCES

- 593 Farmer, D. M., C. L. McNeil and B. D. Johnson, 1993: Evidence for the importance of bubbles in
 594 increasing air-sea gas flux, *Nature*, **361**, 620–623.
 595 Wanninkhof, R., W. E. Asher, D. T. Ho, et al., 2009: Advances in quantifying air-sea gas exchange and
 596 environmental forcing, *Annu. Rev. Mar. Sci.*, **1**, 213–244.
 597 Fuentes, E., H. Coe, D. Green, et al., 2010: Laboratory-generated primary marine aerosol via bubble-
 598 bursting and atomization, *Atmos. Meas. Tech.*, **3**(1), 141–162.

- 599 Zhou, J., K. Mopper and U. Passow, 1998: The role of surface-active carbohydrates in the formation of
600 transparent exopolymer particles by bubble adsorption of seawater, *Limnol. Oceanogr.*, **43**(8), 1860–
601 1871.
- 602 Frouin, R., S. Iacobellis and P.-Y. Deschamps, 2001: Influence of oceanic whitecaps on the global
603 radiation budget, *Geophys. Res. Lett.*, **28**(8), 1523–1526.
- 604 Stramski, D., 1994: Gas microbubbles: An assessment of their significance to light scattering in
605 quiescent seas, *Ocean Optics 12*, edited by J. S. Jaffe, *Proc. SPIE Int. Soc. Opt. Eng.*, **2258**, 704–710.
- 606 Stramski, D. and J. Tegowski, 2001: Effects of intermittent entrainment of air bubbles by breaking wind
607 waves on ocean reflectance and underwater light field, *J. Geophys. Res.*, **106**(C12), 31,345–331,360.
- 608 Zhang, X., M. Lewis and B. Johnson, 1998: Influence of bubbles on the scattering of light in the ocean,
609 *Appl. Opt.*, **37**(27), 6525–6536.
- 610 Ainslie, M. A., 2005: Effect of wind-generated bubbles on fixed range acoustic attenuation in shallow
611 water at 1–4 kHz, *J. Acoust. Soc. Am.*, **118**(6), 3513–3523.
- 612 Terrill, E. J. and W. K. Melville, 2000: A broadband acoustic technique for measuring bubble size
613 distributions: Laboratory and shallow water measurements, *J. Atmos. Oceanic Technol.*, **17**(2), 220–
614 239.
- 615 Deane, G. B. and M. D. Stokes, 2002: Scale dependence of bubble creation mechanisms in breaking
616 waves, *Nature*, **418**(6900), 839–844.
- 617 Czerski, H., M. Twardowski, X. Zhang, et al., 2011: Resolving size distributions of bubbles with radii less
618 than 30 m with optical and acoustical methods, *J. Geophys. Res.*, **116**(C7), 1-13.
- 619 Stokes, M. D. and G. B. Deane, 1999 A new optical instrument for the study of bubbles at high void
620 fractions within breaking waves, *IEEE J. Ocean. Eng.*, **24**(3), 300-311.
- 621 Leifer, I., G. D. Leeuw and L. H. Cohen, 2003: Optical Measurement of Bubbles: System Design and
622 Application, *J. Atmos. Oceanic Technol.*, **20**(9), 1317–1332.
- 623 Thomanek, K., O. Zielinski, H. Sahling, et al., 2010: Automated gas bubble imaging at sea floor – a new
624 method of in situ gas flux quantification, *Ocean Sci.*, **6**(2), 549-562.
- 625 Zielinski, O., B. Saworski and J. Schulz, 2010: Marine bubble detection using optical-flow techniques, *J.*
626 *Eur. Opt. Soc, Rapid Publ.*, **5**(10016s), 1-5.
- 627 Boelmann, J. and O. Zielinski, 2015: Automated characterization and quantification of hydrocarbon
628 seeps based on frontal illuminated video observations *J. Eur. Opt. Soc.-Rapid*, **10**(15018), 1-6.
- 629 Nixon, M. S. and A. S. Aguado, 2002: *Feature Extraction & Image Processing for Computer Vision*,
630 Newnes (an imprint of Butterworth-Heinemann Ltd).
- 631 Wang, B. and S. A. Socolofsky, 2015: A deep-sea, high-speed, stereoscopic imaging system for in situ
632 measurement of natural seep bubble and droplet characteristics, *Deep Sea Res Part 1 Oceanogr Res*
633 *Pap*, **104**, 134–148.
- 634 Honkanen, M., P. Saarenrinne, T. Stoor, et al., 2005: Recognition of highly overlapping ellipse-like
635 bubble images, *Meas. Sci. Technol.* , **16**, 1760–1770.
- 636 Taboada, B., L. Vega-Alvarado, M. S. Córdova-Aguilar, et al., 2006: Semi-automatic image analysis
637 methodology for the segmentation of bubbles and drops in complex dispersions occurring in
638 bioreactors, *Exp. Fluids*, **41**(3), 383-392.
- 639 Zhong, S., X. Zou, Z. Zhang, et al., 2016: A flexible image analysis method for measuring bubble
640 parameters, *Chem. Eng. Sci.*, **141**, 143–153.
- 641 Gonzalez, R. C. and R. E. Woods, 2008: *Digital Image Processing*, Prentice Hall.
- 642 Lee, S. U. and S. Y. Chung, 1990: A comparative performance study of several global thresholding
643 techniques for segmentation, *Comput. Vision Graphics Image Process.*, **52** 171–190.
- 644 Liu, X. and S. Fang, 2015: A convenient and robust edge detection method based on ant colony
645 optimization, *Opt. Commun.*, **353**, 147–157.
- 646 Abdou, I. E. and W. K. Pratt, 1979: Quantitative design and evaluation of enhancement/thresholding
647 edge detectors, *Proc. IEEE*, **67**(5), 753–763.
- 648 Medwin, H., 1970: In situ acoustic measurements of bubble populations in coastal ocean waters, *J.*
649 *Geophys. Res.*, **75**(3), 599–611.

- 650 Medwin, H., 1977: In situ acoustic measurements of microbubbles at sea, *J. Geophys. Res.*, **82**(6), 971–
651 976.
- 652 Geißler, P. and B. Jähne, Measurements of Bubble Size Distributions with an Optical Technique Based
653 on Depth from Focus, Proceedings of Air–Water Gas Transfer, Heidelberg University, Germany, 1995,
654 351–362.
- 655 Jähne, B. and P. Geißler, An imaging optical technique for bubble measurements, Proceedings of Sea
656 Surface Sound '94, University of California, USA, 1994, 290–303.
- 657 Wang, Q. and E. C. Monahan, The influence of salinity on the spectra of bubbles formed in breaking
658 wave simulations, Proceedings of Sea Surface Sound '94, University of California, 1994, 312–319.
- 659 Al-Lashi, R. S., S. R. Gunn, E. G. Webb, et al., 2016: A Novel High Resolution Optical Instrument for
660 Imaging Oceanic Bubbles, *IEEE J. Ocean. Eng.*
- 661 Pascal, R. W., M. J. Yelland, M. A. Srokosz, et al., 2011: A Spar Buoy for High-Frequency Wave
662 Measurements and Detection of Wave Breaking in the Open Ocean, *J. Atmos. Oceanic Technol.*, **28**(4),
663 590–605.
- 664 Leighton, T. G., 1994: *The Acoustic Bubble*, ACADEMIC PRESS LIMITED London, 613pp.
- 665 Deane, G. B. and M. D. Stokes, 1999: Air entrainment processes and bubble size distributions in the
666 surf zone, *J. Phys. Oceanogr.*, **29**(7), 1393–1403.
- 667 Hough, P. V. C., 1962: A Method and Means for Recognizing Complex Patterns.
- 668 Duda, R. O. and E. Hart, 1972: Use of the Hough transform to detect lines and curves in pictures,
669 *Commun. ACM*, **15**(1), 11–15.
- 670 Kimme, C., D. Ballard and J. Sklansky, 1975: Finding circles by an array of accumulators, *Commun.*
671 *ACM*, **18**(2), 120–122.
- 672 Ballard, D. H., 1981: Generalizing the Hough transform to detect arbitrary shapes, *Pattern Recogn.*,
673 **13**(2), 111–122.
- 674 Zheng, Y., M. S. Nixon and R. Allen, 2004: Automated segmentation of lumbar vertebrae in digital
675 videofluoroscopy images, *IEEE Trans. Med. Imag.*, **23**(1), 45–52.
- 676 Walsh, A. L. and P. J. Mulhearn, 1987: Photographic measurements of bubble populations from
677 breaking wind waves at sea, *J. Geophys. Res.*, **92**(C13), 14533–14565.
- 678 Bradski, G. and A. Kaehler, 2008: *Learning OpenCV: [computer vision with the OpenCV library]* O'Reill
679 Media, Inc., Sebastopol, USA, 543pp.
- 680